Biopolymer Templated Glass with a Twist: Controlling the Chirality, Porosity, and Photonic Properties of Silica with Cellulose Nanocrystals

*Kevin E. Shopsowitz, Joel A. Kelly, Wadood Y. Hamad, and Mark J. MacLachlan**

A detailed investigation of the formation and properties of mesoporous silica templated by the chiral nematic liquid crystal phase of cellulose nanocrystals (CNCs) is presented. Under appropriate conditions, CNCs co-assemble with silica up to loadings of ≈60 wt% to give composite films with periodic chiral nanostructures. The periodicity of these films can be readily controlled to obtain materials that selectively reflect light with wavelengths ranging from ≈400–1400 nm. The co-assembly of CNCs and silica into ordered chiral nematic structures is demonstrated to occur within a narrow window of pH and is affected by aging: a slow rate of silica condensation appears to be vital for the formation of well-ordered materials. CNCs can be removed from the composite films by calcination or acid hydrolysis to give high surface area chiral nematic mesoporous silica (CNMS) with tunable pore diameters. The combination of mesoporosity and chiral nematic ordering in CNMS enables it to be used in a unique way for refractometric sensing applications. It is shown that, when using circular dichroism (CD) signals to monitor the chiral photonic properties of CNMS, variations in refractive index can be detected based on changes of both CD signal intensity and peak position with good sensitivity.

1. Introduction

Cellulose is the most abundant organic polymer on Earth and has been used as a material by human civilizations for thousands of years.[1] Due to its virtually unlimited availability, there has been considerable interest recently in developing renewable technologies based on cellulose in areas including biofuel production and nanotechnology.[2,3] The use of cellulose in nanotechnology has been largely driven by the discovery made over 60 years ago that cellulose nanocrystals can be isolated from bulk cellulose through controlled acid hydrolysis.[4] Cellulose nanocrystals (CNCs), or nanocrystalline cellulose, have many interesting properties including their exceptional strength, high surface area, ease of functionalization, and self-assembly properties that have driven research in various directions.[3,5,6]

The chiral structure of CNCs, which ultimately derives from the chirality of their glucose subunits, enables them to form a chiral nematic liquid crystalline (CN-LC) phase when dispersed in various solvents.[7,8] This spontaneous self-assembly process occurs above a critical concentration and is influenced by many factors including the choice of solvent, the aspect ratio of the particles, surface charge, pH, and ionic strength.[8–11] Remarkably, the slow evaporation of water from aqueous CNC suspensions can result in solid films that retain the chiral nematic ordering of the LC phase.[12,13] These films often have brilliant iridescent colors due to the 1D photonic properties of CN-LCs, which cause them to selectively reflect circularly polarized light with wavelengths that depend on the helical pitch of the chiral nematic structure.[14] A variety of methods have been explored to influence the final helical pitch, and hence color, of CNC films. These include the addition of salt to the suspension (leading to a blue shift),[13] ultrasonication of the suspension prior to drying (higher energies lead to a red shift),[15] and varying the drying temperature (increased temperature causes a blue shift).[13]

The use of surfactant molecules, block copolymers, and other lyotropic liquid crystals as templates for ordered mesoporous materials dates back over 20 years.[16–18] The typical amphiphilic templates that are employed in this process generally give hexagonal, cubic, or lamellar mesoporous structures. As an extension of this approach, chiral surfactant molecules have been used to generate chiral hexagonal mesoporous structures.[19,20] Biological macromolecules such as cellulosic derivatives present an interesting alternative to surfactants as chiral templates due to their inherent enantiopurity and ability to form unique liquid crystalline phases. Antonietti and Thomas used hydroxypropylcellulose (HPC) as a template to construct chiral nematic silica/HPC monoliths, but did not retain the chiral nematic order after removing the HPC.[21] The shape, size, and high surface area of CNCs, along with its chiral nematic liquid crystal behavior, make it an attractive template for generating novel chiral mesoporous materials. Dujardin and Mann used CNCs as a template to make CNC/silica composites and removed the

---

Dr. K. E. Shopsowitz, Dr. J. A. Kelly,
Prof. M. J. MacLachlan
Department of Chemistry
University of British Columbia
2036 Main Mall, Vancouver, BC, Canada, V6T 1Z1
E-mail: mmaclach@chem.ubc.ca
Dr. W. Y. Hamad
FPInnovations, 3800 Wesbrook Mall
Vancouver, BC, Canada, V6S 2L9

DOI: 10.1002/adfm.201301737

CNCs by calcination. Although TEM images suggested some nematic order to the pore structure in the materials, long-range chiral ordering was not clearly observed.[22]

Introducing porosity into photonic crystals provides a means to tune their optical properties by infiltrating the pores with various guests. Macroporous photonic crystals are often synthesized by using templates that introduce both the porosity and photonic structure into the material as in the use of monodisperse silica or polymer spheres to template inverse opals.[23–26] Mesoporous photonic crystals have been synthesized using a variety of approaches (e.g., electrochemical etching of silicon, alternate deposition of porous silica and titania layers, self-assembly of mesoporous silica spheres to form opals) and show promise for applications involving sensing, photovoltaics, and light emission.[27–34] The self-assembly of lyotropic liquid crystals has been used to introduce mesoporosity into photonic crystals, however, multiple processing steps are generally required to build up the periodic photonic structure.[33,35] The nanoscale dimensions and chiral nematic self-assembly of CNCs are appealing for the simultaneous templation of both mesoporous and photonic structures in one step.

Recently our group has demonstrated that CNCs can be used to template a variety of different mesoporous materials with chiral nematic structures including silica, organosilica, carbon, and titania.[36–39] These materials are available as free-standing, oriented films with photonic properties. In this article we present a detailed study on the formation of CNC/silica composite and chiral nematic mesoporous silica (CNMS) films with new results regarding the range of silica loadings that can be achieved, the influence of initial pH and aging on CNC/silica self-assembly, the thermal stability of CNMS, and how different methods of removing CNCs affect mesoporosity. These results provide new insights regarding the co-assembly of silica and CNCs, and highlight how the structure of the materials can be varied through changes in both the self-assembly and template removal steps. Furthermore, as a proof of concept, we show that the chiral photonic structure of CNMS films makes them useful for detecting changes in refractive index via circular dichroism (CD). These results demonstrate that both the intensity and position of the CD signal of CNMS materials could form the basis for refractive index-based photonic sensors. Along with having interesting properties in their own right, CNC/silica composites and CNMS materials are also important intermediates for producing other chiral nematic mesoporous materials (e.g., carbon and titania).[38,39] The detailed results presented in this paper further elucidate the scope and limitations of using CNCs as a template, and will help guide the development of other materials through use of these unique biologically derived nanomaterials.

2. Results and Discussion

2.1. Synthesis and Characterization of Chiral Nematic CNC/Silica Composite Films

The cellulose nanocrystals (CNCs) used in our experiments were prepared by sulfuric acid hydrolysis (64 wt% H_2SO_4 at 45 °C for 25 min) of a commercial, fully-bleached Kraft softwood pulp. **Figure 1**a shows a TEM image of negatively-stained CNCs prepared in this manner. Previous work has shown that these conditions give CNCs with 89% crystallinity and a crystallite size of 8.3 nm as determined by powder X-ray diffraction (PXRD).[40] Sulfate ester groups are introduced onto the surface of CNCs during this procedure (i.e., CNC-OH is converted to CNC–OSO_3H) with a conversion of about one sulfate group per 20 glucose units as determined by combustion analysis.[40] This gives the CNC particles a negative surface charge when dispersed in water (with a zeta potential of −59 mV), which stabilizes the colloidal suspension and is also important for the formation of a chiral nematic phase.[9,11] A 3 wt% aqueous CNC suspension with a pH of 2.4 was used for our subsequent experiments unless otherwise noted; the acidic pH of this suspension derives entirely from H^+ associated with the surface sulfate groups of CNCs that remain after extensive dialysis.

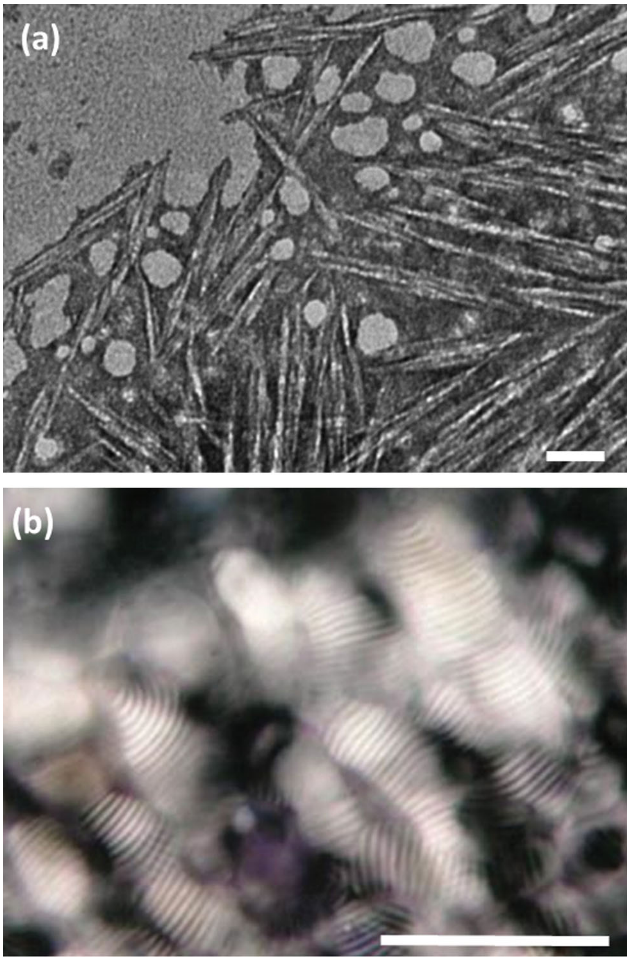

Figure 1. Imaging of CNCs before and during self-assembly with TMOS. a) TEM image of negatively-stained CNC template (scale bar = 100 nm). b) POM image of a drop taken from a CNC/TMOS mixture during evaporation on a glass slide (scale bar = 50 µm).

CNC/silica composite films were prepared through evaporation-induced self-assembly (EISA) of CNCs with tetramethoxysilane (TMOS) as shown in **Scheme 1**. A series of samples was prepared by varying the amount of TMOS used relative to

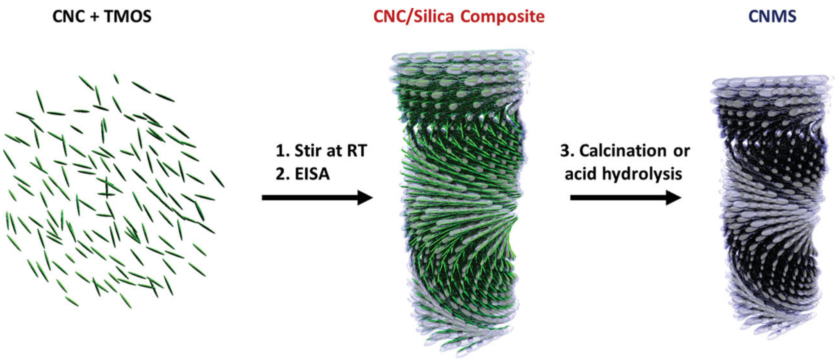

Scheme 1. Synthesis of chiral nematic mesoporous silica from CNCs and TMOS.

CNCs (Comp1-Comp8) and the compositions are reported in **Table 1**. TMOS is at first immiscible when added to an aqueous CNC suspension but quickly dissolves as it is partially hydrolyzed upon stirring for several minutes at room temperature. We tested whether CNCs could form a chiral nematic phase in the presence of TMOS by drop-casting the CNC/TMOS mixtures onto glass microscope slides and observing the evaporation process by polarized optical microscopy (POM, Figure 1b). The initial concentration of the CNC suspension used (3 wt%) is below the critical concentration for anisotropic phase formation and the drops initially appear dark when viewed under crossed polarizers. As evaporation takes place, a fingerprint texture is established demonstrating that the chiral nematic phase of CNCs can form over a wide range of TMOS concentrations (the initial TMOS concentrations that were tested ranged from 0.22 M to 0.74 M).

CNC/silica composite films were formed by casting the homogeneous mixtures in polystyrene Petri dishes and allowing them to dry under ambient conditions. Time-lapse photography of a CNC/TMOS mixture during EISA shows the formation of chiral nematic ordering in the resulting free-standing film, with structural color observed during the last ≈8 h (**Figure 2**). The resulting free-standing films tend to crack into 1–3 cm sized pieces, with typical thicknesses between 50–100 µm. The cracking occurs during the final stages of the drying process (more cracking tends to occur for films with higher silica loadings) due to the formation of pressure gradients, and may be prevented through the addition of additives such as glucose.[41] The weight% of silica in the different composite samples was determined by thermogravimetric analysis (TGA) and ranges from 29% for Comp1 to 58% for Comp8 (see Table 1). It should be noted that the determination of the weight% silica is based on the assumption that the composite materials solely consist of cellulose and fully condensed SiO_2; since the silica is unlikely to be fully condensed, this may lead to a slight overestimation of the CNC content in the samples.

Table 1. Compositions and Properties of CNC/Silica Composites.

Sample	mmol TMOS/150 mg CNC	wt% CNC[a)]	λ_{max} [nm]	P_{UV-Vis} [nm][b)]	P_{SEM} [nm]
CN-CNC	0	100	475	317	350
Comp1	1.09	71	608	405	-
Comp2	1.22	68	708	472	575
Comp3	1.36	65	770	513	-
Comp4	1.69	60	838	559	-
Comp5	2.03	57	929	619	760
Comp6	2.37	51	986	657	-
Comp7	3.05	47	1172	781	-
Comp8	3.73	42	1420	947	920

[a)] Calculated from TGA; [b)] Calculated by dividing λ_{max} by n_{avg}, assumed to be 1.5 for all samples.

The presence of chiral nematic ordering in the CNC/silica composite films was confirmed by scanning electron microscopy (SEM, **Figure 3**), which shows a twisting periodic structure perpendicular to the surface of the films that is similar to what is seen for chiral nematic CNC films without silica (CN-CNC, Figure 3a). This ordering is indicative of a chiral nematic structure with its helical axis oriented perpendicular to the surface of the films (each repeating band corresponds to a half helical pitch of the chiral nematic structure).[42] Chiral nematic periodic structures were observed by SEM for all of the CNC/silica composite samples, further demonstrating that the chiral nematic self-assembly of CNCs is remarkably tolerant to silica loading. From Figure 3, it is also evident that the repeating distance ($P/2$) depends on the silica loading and shows a pronounced increase as the amount of TMOS added relative to CNCs is raised. Average values for P of 350 nm, 575 nm, 760 nm, and 920 nm were measured by SEM for CN-CNC, Comp2, Comp5, and Comp8, respectively. The increase in helical pitch caused by increasing the amount of silica in the composite films may be a result of greater silica wall thickness, although modulation of the electrostatic interactions between CNCs could also play a role. This behavior is the opposite of that previously reported for the addition of salts (e.g., NaCl) to CNCs, which is believed to reduce the helical pitch by masking electrostatic repulsion.[9]

Chiral nematic liquid crystals selectively reflect circularly polarized light with a handedness that matches that of the chiral nematic structure according to:

$$\lambda_{max} = n_{avg} P \sin\theta \tag{1}$$

where n_{avg} is the average refractive index, P is the helical pitch, and θ is the angle between the surface of the liquid crystal and the incident light (for incident light normal to the surface/parallel to the helical axis, $\sin\theta = 1$).[14] For a given angle of incidence, λ_{max} may therefore be tuned by varying the helical pitch or the average refractive index of a chiral nematic liquid crystal. UV-Vis/NIR spectra were collected for samples Comp1-Comp8 and show a continuous red shift of λ_{max} with increased silica loading (Figure 3e). It should be noted that spectra collected from different locations on the same film can vary in λ_{max} values by ≈30 nm. Altogether, λ_{max} of the composite films ranged from 475 nm (for the pure CNC film) to 1420 nm for Comp8 (Table 1). The values for n_{avg} of the different composite materials are essentially constant since the two components,

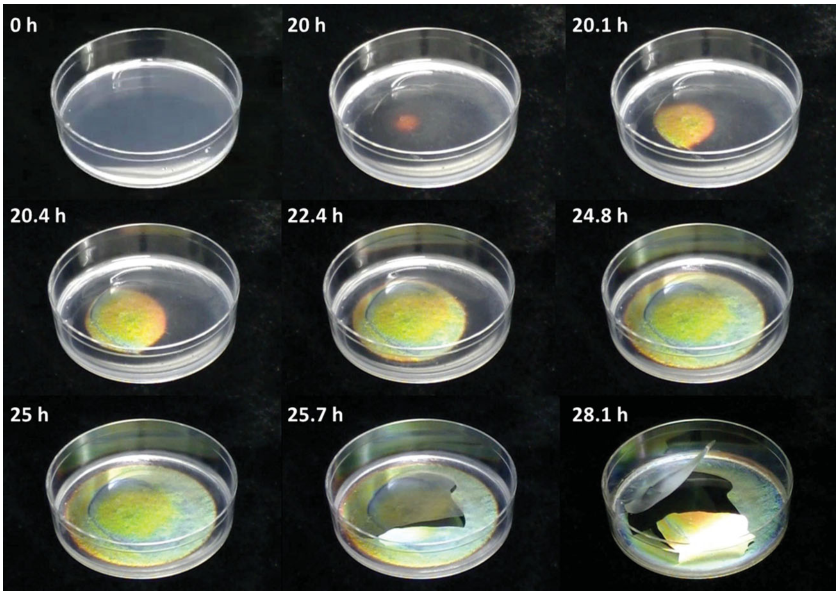

Figure 2. Time-lapse photography of the EISA process for a chiral nematic CNC/silica film.

SiO_2 and crystalline cellulose, have similar refractive indices (n = 1.46 and 1.54, respectively). It can therefore be inferred that the increase in λ_{max} for samples with higher silica content is predominantly caused by the increase in helical pitch observed by SEM. Values of P were also calculated by dividing λ_{max} for the different composite samples by n_{avg}, (assumed to be 1.5 for all samples) and are also reported in Table 1. Although the values of P determined by UV-Vis and SEM both show the same trend of increasing with higher silica loadings, there is some discrepancy that could be caused by uncertainty in the SEM measurements of P due to uneven fracture of the film edge along the helical axis, which is very challenging to eliminate. It is also likely that the helical pitch length and axis are not perfectly uniform throughout the samples, as evidenced by the broad reflectance peaks and defects observed by SEM in some regions.

2.2. Influence of pH and Aging on Composite Film Formation

The considerable tolerance of the chiral nematic self-assembly of CNCs toward TMOS is likely due in part to the fact that the initial pH of the CNC suspensions that were used is near the isoelectric point of colloidal silica

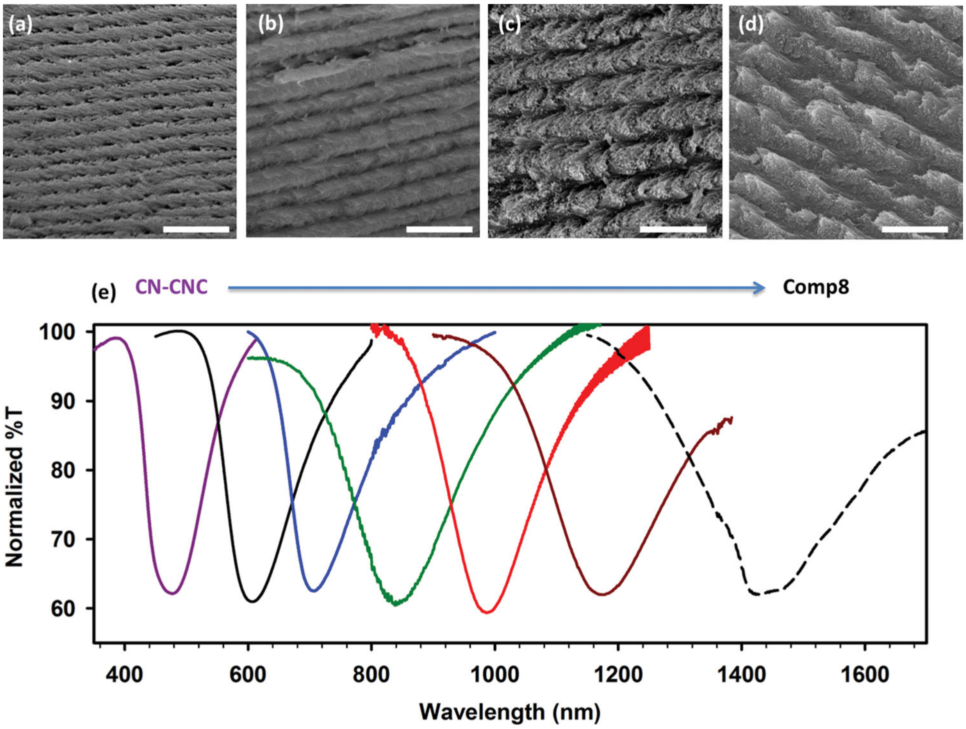

Figure 3. SEM images of chiral nematic CNC and CNC/silica films. a) Cross-sectional image of pure CNC film CN-CNC (scale bar = 1 µm). b) Cross-sectional image of CNC/silica composite film Comp2 at the same magnification as (a) shows a similar periodic structure but with a larger repeating distance (scale bar = 1 µm). c) Cross-sectional image of CNC/silica composite film Comp5 (scale bar = 1 µm). d) Cross-sectional image of CNC/silica composite film Comp8 (scale bar = 1 µm). e) UV-Vis spectra for chiral nematic CNC and CNC/silica composite films (for clarity, Comp3 and Comp5 were not included).

(pH ≈ 2). This is important for two reasons: 1) the chiral nematic self-assembly of CNCs is known to be very sensitive to the presence of charged species[5,9,10] and 2) operating close to the isoelectric point of colloidal silica suppresses silica polymerization.[43] This allows for CNC self-assembly to occur unimpeded with silica condensation mostly occurring at the later stages of the drying process. Previous studies have shown that silanes do not form covalent bonds with cellulose at ambient temperature under these conditions, so the silica is likely only hydrogen bonded to the surface of the CNCs during the drying process.[44] If left unattended for extended periods (days to months), the CNC/TMOS mixtures at pH 2.4 lose their ability to self-assemble into chiral nematic films and eventually gel due to silica condensation. Films cast from the gelled dispersion are opaque white and have a disordered structure revealed by SEM (see the Supporting Information, Figure S1).

The influence of initial pH on composite film formation was investigated by titrating a CNC suspension with HCl or NaOH prior to the addition of TMOS (the same CNC/TMOS ratio reported for Comp3 was used; these samples are denoted as Comp3-pHx). Adjusting the initial pH of the CNC suspension to 2 with HCl completely inhibited the chiral nematic self-assembly of CNCs, resulting in transparent films without photonic properties. POM and SEM observations of Comp3-pH2 do not show any of the texture or periodic structure present in the chiral nematic films prepared at pH 2.4 (**Figure** 4a,b). Instead, POM shows a uniform birefringence and SEM shows aligned rods organized in a disordered layered structure (Figure 4c). These results indicate that the addition of HCl disrupts the chiral nematic assembly of CNCs resulting in what appear to be nematic composite films. Pure CNC films cast from the pH 2 CNC suspension (i.e., without addition of TMOS) also appeared to show nematic ordering, rather than chiral nematic ordering (data not shown), suggesting that the chiral interactions between CNC particles are inhibited at this lower pH.

Increasing the pH to 7 and 12.5 through the addition of NaOH prior to the formation of CNC/silica composite films also resulted in the disruption of self-assembly. It should be noted that these higher pH conditions for forming CNC/silica composites are similar to those that were previously reported by Mann and co-workers to give nematic materials.[22] The Comp3-pH7 films are opaque while the Comp3-pH12.5 films are transparent, and neither show any evidence for chiral nematic ordering (a POM image of a Comp3-pH12.5 film is shown in Figure S2, Supporting Information). Although pure CNC films cast from suspensions with an initial pH of 12.5 also did not show chiral nematic ordering, interestingly, pure CNC films prepared from pH 7 suspensions without the addition of TMOS form uniform iridescent films. The disruption of chiral nematic ordering in the pH 7 composite samples is therefore likely to be related to a change in the silica condensation rate. Taken together, these results demonstrate that the formation of chiral nematic CNC/silica composite films is sensitive to the addition of acid or base, which may disrupt self-assembly by both modulating the interactions between CNC particles and by influencing the rate of silica condensation.

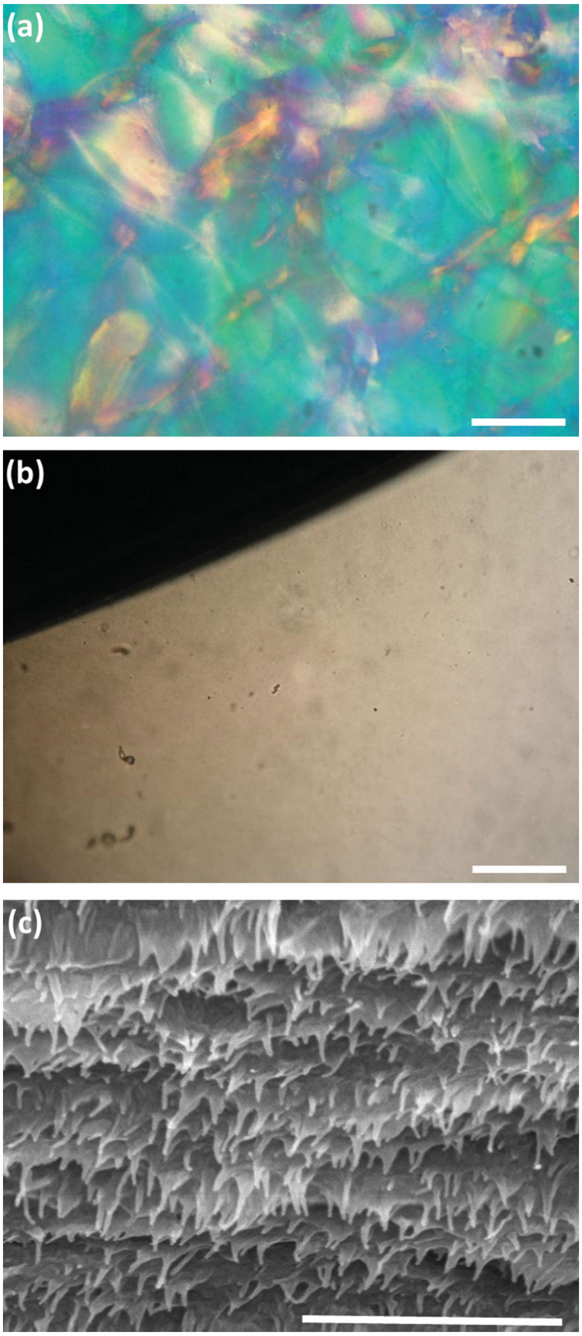

Figure 4. Disruption of chiral nematic ordering by the addition of HCl. a) POM image of a chiral nematic CNC film at pH 2.4 (scale bar = 100 µm). b) POM image of Comp3-pH2 (scale bar = 100 µm). c) Cross-sectional SEM image of Comp3-pH2 (scale bar = 1 µm).

2.3. Removal of CNCs to Generate CNMS with Photonic Properties

The removal of CNCs from CNC/silica composites can be accomplished by calcination or by hydrolysis in the presence of strong acids.[36,39] CNC/silica composite samples Comp1-Comp8 and the Comp3-pHx series were calcined at 540 °C

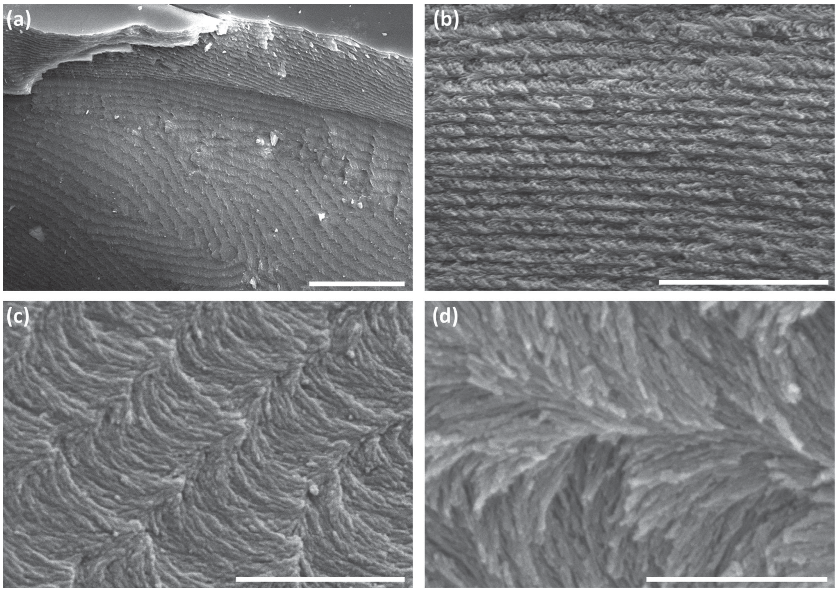

Figure 5. SEM images of selected CNMS samples. a) Cross-sectional image of film showing repeating structure with various defects (CNMS6, scale bar = 10 μm). b) Cross-sectional view of CNMS2 (scale bar = 2 μm). c) High magnification image of CNMS2 showing left-handed structure (scale bar = 1 μm). d) High magnification image of CNMS3-HCl (scale bar = 500 nm).

under flowing air to give silica samples denoted as CNMS1-CNMS8 and MS3-pHx, respectively. CNCs were also removed from Comp3 using 12 M HCl and 6 M H_2SO_4 at 85–100 °C to give materials denoted as CNMS3-HCl and CNMS3-H_2SO_4, respectively. The removal of CNCs from the composite films can be confirmed by TGA, IR, and PXRD as reported previously.[36,39] Comparing the IR spectra for CNMS3 and CNMS3-HCl, we observe a peak at 960 cm^{-1} for the CNMS3-HCl sample that is not present in the calcined sample (Figure S3a,b, Supporting Information). This peak can be assigned to Si–OH stretching indicating that the silica network in the acid hydrolyzed sample is not fully condensed.[45] This was further confirmed by TGA, which shows a small weight loss (ca. 4 wt%) between 450–600 °C that is suggestive of further silica condensation (Figure S3d, Supporting Information).

SEM confirmed the retention of chiral nematic organization in the pure silica films produced through calcination and acid hydrolysis of CNCs (**Figure 5**). The top surfaces of the films appear very smooth, but perpendicular to the surface the periodic helical pitch characteristic of chiral nematic organization is observed. In some locations we see a fingerprint texture that corresponds to a condensed version of that observed by POM in the LC phase (Figure 5a). This demonstrates that the liquid crystalline organization of CNCs is locked into place and faithfully replicated in the pure silica samples. The SEM images of CNMS films also indicate that contraction of the helical pitch occurs during calcination. For example, P_{avg} measured for CNMS2 and CNMS5 are 307 nm and 415 nm, respectively, compared to 575 nm and 760 nm for the corresponding composite samples Comp2 and Comp5. At very high magnification a twisting rod-like morphology is resolved, resembling images of pure CNC films. Throughout the samples, this twisting occurs in a counter-clockwise direction when looking down the helical axis, consistent with a left-handed helical organization (Figure 5c,d).

The presence of chiral nematic ordering in the silica films after the removal of CNCs endows them with their unique chiral photonic properties. The pure chiral nematic silica films show strong birefringence by POM (**Figure 6**) and a texture that is very similar to that observed for pure chiral nematic CNC films (Figure 4a). The calcined chiral nematic silica films selectively reflect light at wavelengths that are blue-shifted by ≈250–300 nm compared to the corresponding CNC/silica composite films. This blue shift results from the combination of a decrease in average refractive index upon the removal of cellulose as well as the contraction in helical pitch discussed above. The use of acid hydrolysis to remove CNCs, however, appears to avoid this contraction with the reflectance peak for CNMS3-HCl being red-shifted by ≈150 nm compared to calcined CNMS3 (Figure S4, Supporting Information). Altogether, the series of silica films CNMS1–8 have reflection peaks that range from ≈300–1100 nm (see the Supporting Information, Table S1). Starting from the composite films Comp3–6, mesoporous silica films CNMS3–6 that reflect light at different wavelengths across the entire visible spectrum were obtained. The colors of the films are easily observed by the naked eye and show an angle dependence because of the sinθ dependence of λ_{max} for chiral nematic ordering. CD spectra of the colored films give very intense positive signals with positions that correspond to the colors of the films (Figure 6). This demonstrates that the observed colors arise from the selective reflection of left-handed circularly polarized light as is expected for a left-handed chiral nematic structure.

2.4. Factors Affecting the Mesoporosity of CNMS

Nitrogen adsorption measurements were carried out on selected calcined samples along with the samples prepared with hydrochloric and sulfuric acid (Table S2 and **Figure 7**). The calcined CNMS samples that were measured display type IV adsorption isotherms, which are characteristic of mesoporous materials, and have Brunauer-Emmett-Teller (BET) surface areas ranging from 470–690 m^2 g^{-1} and pore volumes of 0.42–0.63 cm^3 g^{-1}, depending on the CNC/silica ratio of the starting composite materials. The hysteresis in the isotherms can be classified as type H2, which is indicative of a complex pore structure composed of interconnected networks of pores of different size and shape.[46] As expected, the specific surface area and pore volumes of the samples both decrease with increased silica loading (the thicker silica walls make the materials more dense).

The BJH (Barrett-Joyner-Halenda model) pore size distributions for the calcined CNMS samples give peak pore diameters of ≈3 nm, and show very little pore volume past 10 nm

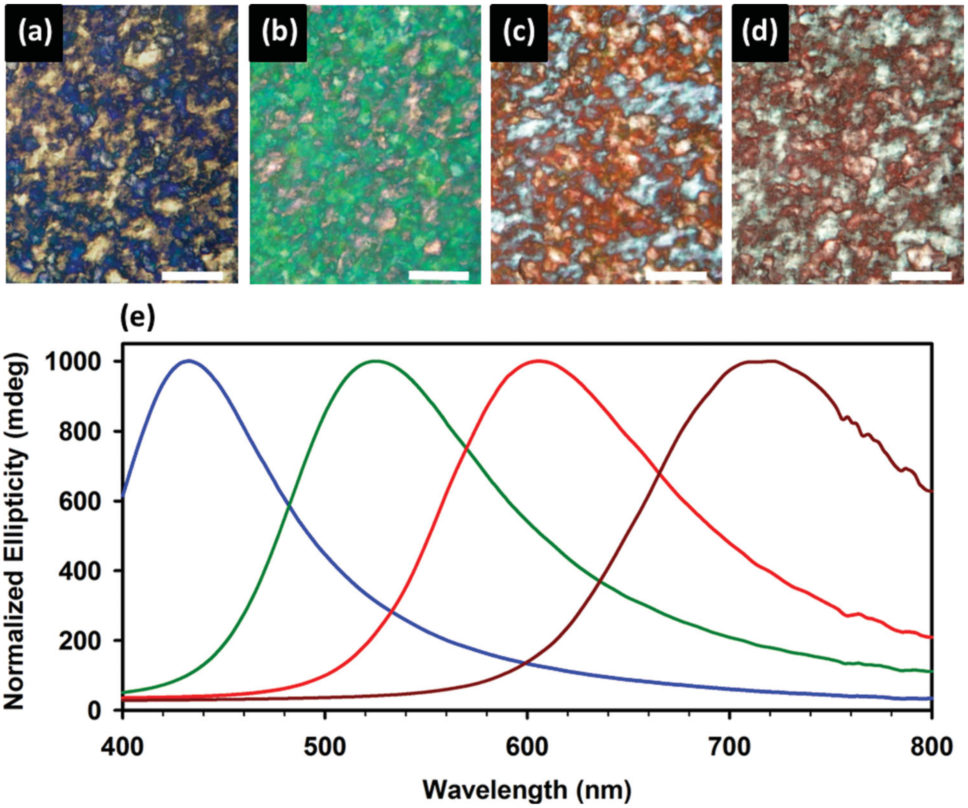

Figure 6. Optical characterization of iridescent silica films CNMS3–6. a–d) Polarized optical images for CNMS3–6 (scale bars = 100 µm). e) Circular dichroism spectra for CNMS3 (blue), CNMS4 (green), CNMS5 (red), and CNMS6 (dark red).

diameter (Figure S5, Supporting Information). This pore size is somewhat smaller than the width distribution measured for the CNC template by TEM, which is centered at around 8 nm (Figure S6, Supporting Information). This observation is consistent with the considerable contraction in helical pitch that occurs during calcination that was measured by UV-Vis and SEM. The pore contraction appears to depend to some extent on the silica loading with the pore size distribution for CNMS1 being slightly broader and having a smaller peak diameter compared to CNMS3 and CNMS6.

Nitrogen adsorption studies were also performed on the calcined silica films MS3-pH2 and MS3-pH12.5. MS3-pH2 displays a type IV isotherm with a similar shape to that of CNMS3. The BET surface area and pore volume calculated for MS3-pH2 are somewhat lower than for CNMS3 (Table S2, Supporting Information). Although it is possible that the lack of chiral nematic ordering for MS3-pH2 may result in a more disordered pore structure that leads to decreased porosity, it is not possible to conclude this for certain since other factors related to pH (e.g., degree of silica condensation) may also play a role. In contrast, MS3-pH12.5 has a considerably lower pore volume and BET surface area compared to the other samples and an isotherm that is characteristic of a macroporous material (Figure 7d) suggesting that CNCs aggregated at this higher pH.

The choice of conditions for removing CNCs from the composite films also has a strong influence on the porosity of the resulting silica materials, which can be exploited for the hard templating of chiral nematic materials such as titania.[39] Nitrogen adsorption measurements for CNMS3-HCl and CNMS3-H_2SO_4 reveal that they have significantly larger pores compared to the calcined CNMS samples. The pore volume and BJH pore diameter of CNMS3-HCl are 1.0 $cm^3\ g^{-1}$ and 11 nm, respectively (Supporting Information, Table S2, Figure S5c). Compared to the calcined samples, the pore volume of CNMS3-HCl is much closer to the theoretical pore volume of 1.15 $cm^3\ g^{-1}$ calculated using the weight% of CNCs in Comp3 (65%) and a density for CNCs of 1.6 g cm^{-3}.[5] Furthermore, the pore size distribution of CNMS3-HCl more closely matches the width distribution of the CNC template measured by TEM (Figure S6, Supporting Information). This more accurate replication of CNC width in the pore structure CNMS3-HCl is also reflected by the fact that little to no helical pitch contraction occurred when CNCs were removed using these conditions (Table S1, Supporting Information). The use of sulfuric acid to remove the CNC template gives a mesoporous material (CNMS3-H_2SO_4) with an even larger pore volume than CNMS3-HCl (1.22 cm^3/g) and a very broad pore size distribution centered around 22 nm (Figure S5d, Supporting Information), which we believe is caused by silica dissolution that occurs under these conditions. In comparison, we have previously prepared ethane-bridged chiral nematic mesoporous organosilicates using these same conditions (6 M H_2SO_4/100 °C) and obtained materials with slightly smaller pore sizes (≈9 nm) than CNMS3-HCl,[37] likely due to the greater hydrothermal stability of the organosilica.[47]

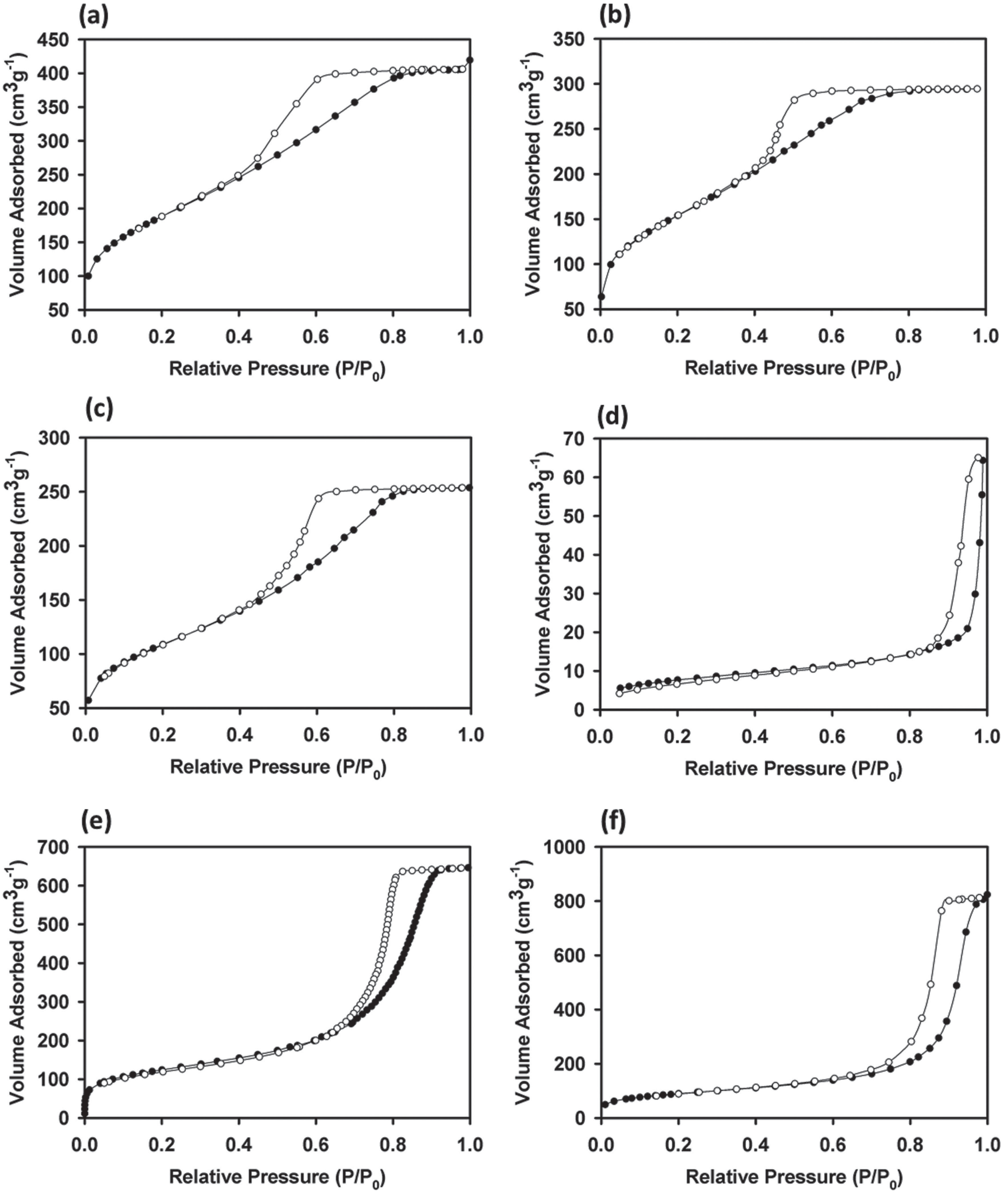

Figure 7. Nitrogen adsorption/desorption isotherms (77 K) for selected samples a) N_2 isotherm for CNMS1. b) N_2 isotherm for CNMS3. c) N_2 isotherm for MS3-pH2. d) N_2 isotherm for MS3-pH12.5. e) N_2 isotherm for CNMS3-HCl. f) N_2 isotherm for CNMS3-H_2SO_4. For all plots black circles represent adsorption and white circles represent desorption.

Transmission electron microscopy (TEM) images taken at different angles for CNMS3-HCl allow for direct visualization of the mesopore structure. Images were taken at angles ranging from –60 to +60 degrees and, after image alignment, were compiled into an AVI (see Video in the Supporting Information). The silica rods that were observed by SEM are seen to be separated by highly anisotropic mesopores with local nematic ordering. The irregular shape and imperfect alignment of the pores appears to give them a high interconnectivity explaining how these chiral nematic pore structures can be readily replicated in other materials through hard templating.[38,39]

2.5. Thermal Stability of CNMS

The chiral nematic mesoporous silica is stable for years under ambient conditions, showing virtually no change in properties after more than two years of storage. At elevated temperature, however, pore collapse may be expected. Thermal stabilities of the mesoporous silica samples CNMS3-HCl and CNMS3 were investigated by measuring N_2 adsorption after heating the samples to different temperatures. When CNMS3-HCl is heated to 540 °C under air, there is only a small decrease in porosity with the BJH pore diameter remaining near 11 nm (Table S2, Figure S5e, Supporting Information). These results demonstrate that the smaller pores observed for the calcined CNMS samples are not simply caused by thermal instability of the structure at this temperature. One possibility is that the structural collapse that occurs during calcination may in part be due to the buildup of pressure from volatile species generated from cellulose decomposition. The porosity of calcined CNMS3 was also measured after heating to 900 °C and 1000 °C for 10 h under nitrogen. Upon heating to 900 °C, partial pore collapse occurs with decreases of BET surface area and pore volume from 556 $m^2 g^{-1}$ and 0.46 $cm^3 g^{-1}$ to 294 $m^2 g^{-1}$ and 0.16 $cm^3 g^{-1}$, respectively. In addition, a large increase in microporosity from 3 $m^2 g^{-1}$ to 178 $m^2 g^{-1}$ was observed. Despite this reduction in mesoporosity, the films retain their iridescence. On the other hand, heating to 1000 °C causes a complete collapse of the chiral nematic pore structure leading to negligible surface area and pore volume and a corresponding loss of iridescence.

2.6. Exploiting the Chiral Photonic Properties of CNMS for Refractive Index Sensing

The combination of porosity and chiral nematic photonic properties in CNMS materials is intriguing for use as a refractive index-based sensor. When immersed in water and other liquids, the films rapidly become transparent and colorless, as shown in **Figure 8**a. A similar effect has also been reported for other porous photonic nanostructures, such as silica inverse opals or helical inorganic nanostructures prepared by glancing angle deposition (GLAD), and has been attributed to approximate refractive index matching between the isotropic liquid in the pores and the walls of the material.[48,49] The birefringence of the mesoporous films is also drastically reduced when the pores are filled with isotropic liquids. These changes are reversible and the films fully regain their iridescence and birefringence upon drying (Figure 8a). As the silica in these materials is amorphous, the birefringence of the films results entirely from the anisotropic shape of the pores (known as form birefringence), and is dependent on the refractive index contrast between the pores and the silica. This is in contrast to the materials that contain CNCs, since CNCs have an anisotropic crystalline structure and are therefore intrinsically birefringent.

As the refractive index of water ($n = 1.33$) and SiO_2 ($n = 1.46$) are not perfectly matched, a residual peak is expected after water infiltration; it is too small, however, to be detected by transmission spectra (Figure S7, Supporting Information). The chiral origin of the reflectance peak allows optical changes in the films to be probed using circular dichroism. The CD signal of the films is reduced by two orders of magnitude to ≈30 mdeg after infiltration with water (Figure 8b). The CD peak is also red-shifted compared to the reflectance peak for the dry film as expected from an increase in n_{avg}. Increasing the refractive index by infiltration with a range of aqueous sucrose solutions (a common approach to test the sensitivity of refractive index-based sensors) shows a gradual decrease in CD signal and red-shift in maximum wavelength (Figure 8c). The sensitivities of the mesoporous silica in CD signal intensity and peak position toward changes in refractive index are ≈200 mdeg/refractive index unit (RIU) and ≈170 nm/RIU, respectively, which is comparable to the sensitivity of porous silicon-based photonic sensors based on reflectivity measurements.[50] These results suggest that there are opportunities to employ these materials in optical sensing applications where small changes in the refractive index within the pores would result in changes in both the intensity and position of the CD peak. This takes advantage of the increased sensitivity of circular dichroism over conventional transmission or reflectivity measurements and the unique combination of chirality, photonic properties and mesoporosity in these materials.

3. Conclusions

We have discovered that cellulose nanocrystals can be used to form composite materials with silica that have tunable photonic properties. These materials are formed using a simple self-assembly approach and have a left-handed chiral nematic structure. The chiral nematic self-assembly of the acid form of sulfated CNCs is remarkably tolerant to the presence of TMOS and chiral nematic composite films with up to 58% silica were obtained. On the other hand, the synthesis of chiral nematic composite films is very sensitive to the addition of extra acid or base, which may disrupt the self-assembly of CNCs by modulating their electrostatic interactions and/or increasing the rate of silica condensation. Based on these considerations, we suggest that it should be possible for CNCs to template a wide variety of different materials as long as the precursors are not strongly acidic or basic, are hydrophilic, and can be prevented from fully condensing until the later stages of EISA.

The removal of the CNC template from CNC/silica composite films can be carried out by calcination or acid hydrolysis to give free-standing chiral nematic mesoporous silica films. The method of removing the CNC template from the composites has a strong influence on the porosity of the resulting silica material; pore diameters of 3 nm, 11 nm, and 22 nm were obtained by using three different procedures. This large range of pore sizes may be attributed to differing amount of contraction and silica dissolution that occur depending on the CNC removal method. This ability to control the mesopore size over such a wide range could be useful for many applications.

The combination of chiral nematic ordering and porosity in CNMS materials causes their colors to respond to changes in refractive index within the mesopores, a property that could make them useful as "smart windows" or sensors. The fact that the reflected signal is exclusively left-handed circularly polarized allows for small changes in refractive index within the films to be probed by circular dichroism; by subtracting the right-handed signal, background noise can be effectively eliminated and thus the sensitivity increased.

CNCs exhibit chirality at three different levels: the molecular chirality of individual glucose units, the chiral shape of individual crystallites, and the long-range chirality present in the

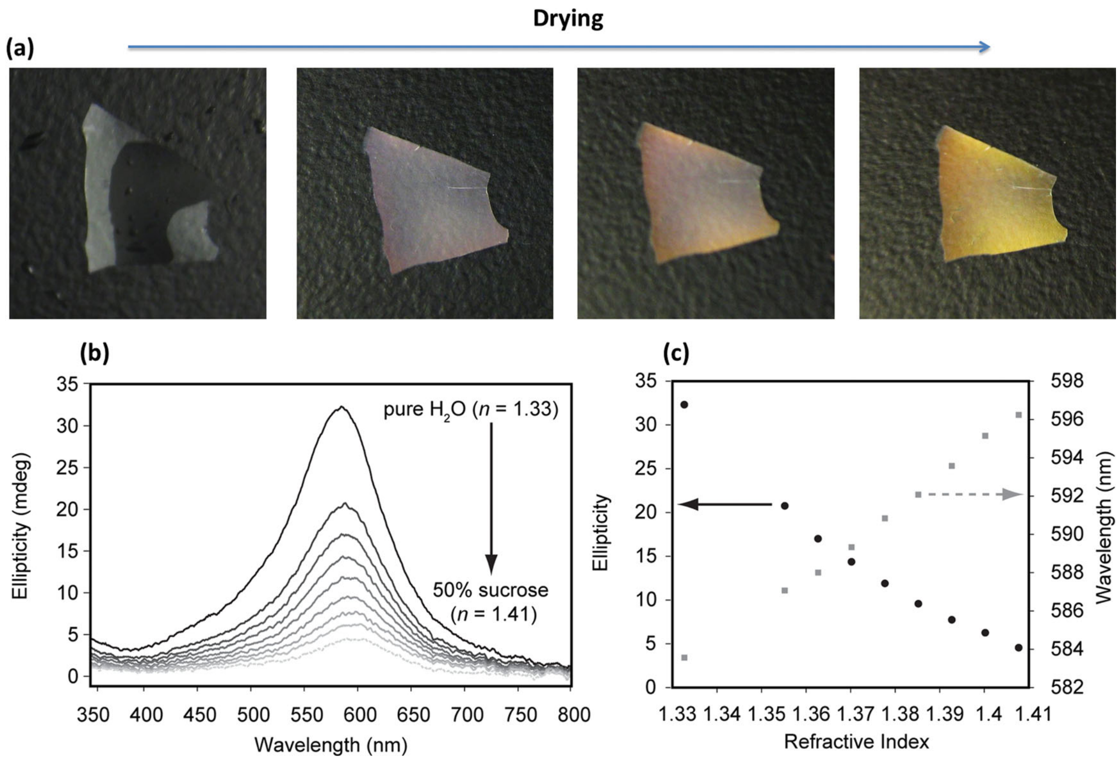

Figure 8. Effect of refractive index changes on the photonic properties of CNMS films. a) Series of photographs showing the reversible color change that occurs upon wetting and drying a CNMS film. b) Circular dichroism spectra of a CNMS film at different sucrose concentrations ranging from 0–50 wt%. c) Plots of peak intensity and position vs refractive index for the series of CD spectra shown in (b).

chiral nematic liquid crystalline phase. Although it is clear that long-range chirality exists in CNMS, it is still uncertain whether these other levels of chirality are replicated. The optimization of short-range chirality is likely to be important if CNMS materials are to find use in applications such as chiral separation. Future work will aim to further understand the pore structure of these materials and investigate whether their chirality makes them useful for enantioselective separation. Finally, the wide availability of cellulose (CNCs are beginning to be produced at several pilot plants on a multi-ton/day scale) combined with the simplicity of our approach make it plausible that bulk quantities of CNMS could be produced at a relatively low cost.

4. Experimental Section

General: All solvents and reagents including TMOS (tetramethyl orthosilicate, Acros) were purchased from commercial sources and used without further purification. Thermogravimetric analysis was performed on a PerkinElmer Pyris 6 thermogravimetric analyzer. All samples were run under air. Gas adsorption studies were performed at 77 K using a Micromeritics ASAP 2000 gas sorption analyzer. All samples were degassed for 2 hours under vacuum at 100 °C immediately prior to analysis. BJH (Barrett-Joyner-Halenda model) pore size distributions were all calculated from the adsorption branch of the isotherm. IR spectra were obtained with a Nicolet 6700 FT-IR equipped with a Smart Orbit diamond ATR. Powder X-ray diffraction patterns were collected using a D8 advance X-ray diffractometer.

Optical Characterization: UV-visible/near-IR spectroscopy was conducted on a Cary 5000 UV-Vis/NIR spectrophotometer. Transmission spectra were collected by mounting free-standing films so that the surfaces of the films were perpendicular to the beam path (pieces of film were taken from near the center of the Petri dishes where they formed, where the films are typically most uniform). The maximum transmittance was set to 100% in a region away from the reflectance peak. CD experiments were performed using a JASCO J-710 spectropolarimeter. Spectra of dry films were collected by mounting samples such that the surfaces of the films were perpendicular to the beam path. For the dry films, small pieces were used that did not completely cover the aperture, as the CD signals from larger pieces are too intense and saturate the detector. The CD signals measured for the dry films were all normalized for the purpose of comparison. Because the intensity for the wet films is drastically reduced compared to the dry films, quantitative comparison of CD signal intensity from wet films was possible through mounting samples large enough to completely cover the aperture inside of a quartz cuvette. Aqueous solutions varying in refractive index from 1.33 to 1.41 were prepared by dissolving sucrose from 0–50 wt% in water.

Microscopy: TEM images of CNCs were collected on a Hitachi H7600 transmission electron microscope at an accelerating voltage of 100 kV. Samples were prepared by dropcasting a dilute CNC suspension onto a carbon-coated TEM grid followed by negatively staining with uranyl acetate. TEM images of mesoporous silica were collected on an FEI Tecnai G2 transmission electron microscope. Samples were prepared by first grinding the films into a fine powder, suspending them in ethanol, and then dropcasting them onto a carbon-coated TEM grid. Ninety-nine images were collected between angles of –60 and +60 degrees at an accelerating voltage of 200 kV. The images were aligned and then compiled into an AVI file. SEM images were collected on a Hitachi S4700 FE-SEM. Samples were prepared by breaking the films into small pieces and attaching them to aluminum stubs using double-sided adhesive tape. The samples were then sputter-coated with 5 nm of either gold or gold-palladium. Polarized optical microscopy was performed on an

Olympus BX41 microscope. All images were taken with the polarizers in a perpendicular (crossed) arrangement unless otherwise noted.

Preparation of Cellulose Nanocrystals: For the preparation of cellulose nanocrystals (CNCs) fully-bleached, commercial Kraft softwood pulp was first milled to pass through a 0.5-mm screen in a Wiley mill to ensure particle size uniformity and to increase surface area. The milled pulp was hydrolyzed in sulfuric acid (8.75 mL of sulfuric acid solution/g pulp) at a concentration of 64 wt.% and a temperature of 45 °C with vigorous stirring for 25 min. The cellulose suspension was then diluted with cold de-ionized (DI) water (≈10 times the volume of the acid solution used) to stop the hydrolysis, and allowed to settle overnight. The clear top layer was decanted and the remaining cloudy layer was centrifuged. The supernatant was decanted and the resulting thick white suspension was washed 3 times with DI water to remove all soluble cellulosic materials. The thick white suspension obtained after the last centrifugation step was placed inside dialysis membrane tubes (12 000–14 000 molecular weight cut-off) and dialyzed against slow running DI water, for 1–4 d. The membrane tubes containing the extracted cellulose materials were placed periodically in DI H_2O, and the procedure was continued until the pH of the water became constant over a period of one hour. The suspension from the membrane tubes was dispersed by subjecting it to ultrasound treatment in a Fisher Sonic Dismembrator (Fisher Scientific) for 10 min at 60% power and then diluted to the desired concentration (3 wt%). The final CNC suspension was measured to have a zeta potential of –59 mV and a pH of 2.4.

Preparation of CNC/Silica Composite Films: In a typical procedure, chiral nematic CNC/silica composite films were prepared by first sonicating a 3 wt% aqueous CNC suspension for 10 min. TMOS was then added dropwise to the suspension and the mixture was left to stir at room temperature for 1 h to obtain a homogeneous solution. (Note that although TMOS was used exclusively in this study, we have found that TEOS can also be used with very similar results. However, when using TEOS in place of TMOS, stirring at elevated temperature or the addition of ethanol is required in order to obtain a homogeneous mixture due to the slower rate of hydrolysis.) The CNC/TMOS mixtures were then poured into polystyrene Petri dishes (5 mL/60 mm diameter dish) and left to dry under ambient conditions (typically 18–24 h were required for complete drying). The different ratios of CNC/TMOS used for the different chiral nematic composite samples (Comp1–8) are listed in Table 1. Chiral nematic CNC films (CN-CNC) were prepared using the same procedure, except without the addition of TMOS. For the samples prepared at different initial pH (Comp3-pHx), the pH of the 3 wt% CNC suspension was adjusted using either 1 M $HCl_{(aq)}$ or 1 M $NaOH_{(aq)}$ prior to the addition of TMOS. Otherwise, the procedure was identical to that used to prepare the other composite samples.

Preparation of Mesoporous Silica by Calcination: For calcination of the CNC/silica composite films, the films were heated under flowing air at a rate of 2 °C min^{-1} to 100 °C, held at that temperature for 2 h, then heated to 540 °C at 2 °C min^{-1} and held at that temperature for 6 h. After slowly cooling the samples to room temperature, free-standing mesoporous silica films were recovered. The yield depended on the proportion of CNCs incorporated.

Preparation of Mesoporous Silica by Acid Hydrolysis: For the removal of CNCs by acid hydrolysis, the composite films (≈600 mg) were placed in 900 mL of either 12 M hydrochloric acid or 6 M sulfuric acid and heated to between 85–100 °C for 18 h (this was done without stirring in order to avoid breaking the films). The films were then filtered, washed with 1 L of water, and alternately washed with a room-temperature piranha solution (20 mL 30% H_2O_2/100 mL H_2SO_4) and water until they appeared colorless. The films were then rinsed with 2 L of water and air-dried.

Supporting Information

Supporting Information is available from the Wiley Online Library or from the author.

Acknowledgements

The authors thank NSERC and FPInnovations for support. K.E.S. and J.A.K. thank NSERC for a postgraduate scholarship and postdoctoral fellowship, respectively. M.J.M. is grateful to NSERC for an EWR Steacie Memorial Fellowship.

Received: May 22, 2013
Revised: June 26, 2013

[1] D. Klemm, B. Heublein, H. P. Fink, A. Bohn, *Angew. Chem. Int. Ed.* **2005**, *44*, 3358.
[2] L. R. Lynd, M. S. Laser, D. Brandsby, B. E. Dale, B. Davison, R. Hamilton, M. Himmel, M. Keller, J. D. McMillan, J. Sheehan, C. E. Wyman, *Nat. Biotechnol.* **2008**, *26*, 169.
[3] D. Klemm, F. Kramer, S. Moritz, T. Lindström, M. Ankerfors, D. Gray, A. Dorris, *Angew. Chem. Int. Ed.* **2011**, *50*, 5438.
[4] B. G. Ranby, *Acta Chem. Scand.* **1949**, *3*, 649.
[5] Y. Habibi, L. A. Lucia, O. J. Rojas, *Chem. Rev.* **2010**, *110*, 3479.
[6] For recent work with CNC, see: a) M. J. D. Clift, E. J. Foster, D. Vanhecke, D. Studer, P. Wick, P. Gehr, B. Rothen-Rutishauser, C. Weder, *Biomacromolecules* **2011**, *12*, 3666; b) K. L. Dagnon, K. Shanmuganathan, C. Weder, S. J. Rowan, *Macromolecules* **2012**, *45*, 4707; c) H. Yang, A. Tejado, N. Alam, M. Antal, T. G. M. van de Ven, *Langmuir* **2012**, *28*, 7834; d) S. Eyley, S. Shariki, S. E. C. Dale, S. Bending, F. Marken, W. Thielemans, *Langmuir* **2012**, *28*, 6514; e) C. Olivier, C. Moreau, P. Bertoncini, H. Bizot, O. Chauvet, B. Cathala, *Langmuir* **2012**, *28*, 12463; f) R. Silva, J. Al-Sharab, T. Asefa, *Angew. Chem. Int. Ed.* **2012**, *51*, 7171; g) J. Majoinen, A. Walther, J. R. McKee, E. Kontturi, V. Aseyev, J. M. Malho, J. Ruokolainen, O. Ikkala, *Biomacromolecules* **2011**, *12*, 2997; h) C. M. Cirtiu, A. F. Dunlop-Briere, A. Moores, *Green Chem.* **2011**, *13*, 288; i) N. Lin, A. Dufresne, *Biomacromolecules* **2013**, *14*, 871; j) I. Kalashnikova, H. Bizot, P. Bertoncini, B. Cathala, I. Capron, *Soft Matter* **2013**, *9*, 952.
[7] J. F. Revol, H. Bradford, J. Giasson, R. H. Marchessault, D. G. Gray, *Int. J.Biol. Macromol.* **1992**, *14*, 170.
[8] L. Heux, G. Chauve, C. Bonini, *Langmuir* **2000**, *16*, 8210.
[9] X. M. Dong, T. Kimura, J. F. Revol, D. G. Gray, *Langmuir* **1996**, *12*, 2076.
[10] X. M. Dong, D. G. Gray, *Langmuir* **1997**, *13*, 2404.
[11] X. M. Dong, J. F. Revol, D. G. Gray, *Cellulose* **1998**, *5*, 19.
[12] J. F. Revol, L. Godbout, D. G. Gray, *J. Pulp Pap. Sci.* **1998**, *24*, 146.
[13] J. Pan, W. Hamad, S. K. Straus, *Macromolecules* **2010**, *43*, 3851.
[14] H. De Vries, *Acta Crystallogr.* **1951**, *4*, 219.
[15] S. Beck, J. Bouchard, R. Berry, *Biomacromolecules* **2011**, *12*, 167.
[16] a) C. T. Kresge, M. E. Leonowicz, W. J. Roth, J. C. Vartuli, J. S. Beck, *Nature* **1992**, *359*, 710; b) J. S. Beck, J. C. Vartuli, W. J. Roth, M. E. Leonowicz, C. T. Kresge, K. D. Schmitt, C. T. W. Chu, D. H. Olson, E. W. Sheppard, S. B. McCullen, J. B. Higgins, J. L. Schlenker, *J. Am. Chem. Soc.* **1992**, *114*, 10834.
[17] a) Q. S. Huo, D. I. Margolese, G. D. Stucky, *Chem. Mater.* **1996**, *8*, 1147; b) D. Y. Zhao, J. L. Feng, Q. S. Huo, N. Melosh, G. H. Fredrickson, B. F. Chmelka, G. D. Stucky, *Science* **1998**, *279*, 548.
[18] For recent examples see: a) C. Xiao, N. Fujita, K. Miyasaka, Y. Sakamoto, O. Terasaki, *Nature* **2012**, *487*, 349; b) M. Guan, W. Wang, E. J. Henderson, O. Dag, C. Kuebel, V. S. K. Chakravadhanula, J. Rinck, I. L. Moudrakovski, J. Thomson, J. McDowell, A. K. Powell, H. Zhang, G. A. Ozin, *J. Am. Chem. Soc.* **2012**, *134*, 8439; c) K. Ma, H. Sai, U. Wiesner, *J. Am. Chem. Soc.* **2012**, *134*, 13180; d) O. Dag, E. J. Henderson, W. Wang,

J. E. Lofgreen, S. Petrov, P. M. Brodersen, G. A. Ozin, *J. Am. Chem. Soc.* **2011**, *133*, 17454; e) S. Das, T. Asefa, *ACS Catal.* **2011**, *1*, 502; f) R. Silva, A. V. Biradar, L. Fabris, T. Asefa, *J. Phys. Chem. C* **2011**, *115*, 22810; g) W. Yang, T.-P. Fellinger, M. Antonietti, *J. Am. Chem. Soc.* **2011**, *133*, 206; h) W. C. Yoo, A. Stein, *Chem. Mater.* **2011**, *23*, 1761.

[19] a) S. Che, A. E. Garcia-Bennett, T. Yokoi, K. Sakamoto, H. Kunieda, O. Terasaki, T. Tatsumi, *Nat. Mater.* **2003**, *2*, 801; b) S. Che, Z. Liu, T. Ohsuna, K. Sakamoto, O. Terasaki, T. Tatsumi, *Nature* **2004**, *429*, 281.

[20] For other examples of chiral templated silica see: a) A. Gabashvili, D. D. Medina, A. Gedanken, Y. Mastai, *J. Phys. Chem. B* **2007**, *111*, 11105; b) S. Fireman-Shoresh, D. Avnir, S. Marx, *Chem. Mater.* **2003**, *15*, 3607; c) S. Fireman-Shoresh, I. Popov, D. Avnir, S. Marx, *J. Am. Chem. Soc.* **2005**, *127*, 2650; d) T. Delclos, C. Aimé, E. Pouget, A. Brizard, I. Huc, M. H. Delville, R. Oda, *Nano Lett.* **2008**, *8*, 1929.

[21] A. Thomas, M. Antonietti, *Adv. Funct. Mater.* **2003**, *13*, 763.

[22] E. Dujardin, M. Blaseby, S. Mann, *J. Mater. Chem.* **2003**, *13*, 696.

[23] O. D. Velev, T. A. Jede, R. F. Lobo, A. M. Lenhoff, *Nature* **1997**, *389*, 447.

[24] B. T. Holland, C. F. Blanford, A. Stein, *Science* **1998**, *281*, 538.

[25] R. C. Schroden, M. Al-Daous, C. F. Blanford, A. Stein, *Chem. Mater.* **2002**, *14*, 3305.

[26] K. Busch, S. John, *Phys. Rev. E* **1998**, *58*, 3896.

[27] Y. Y. Li, F. Cunin, J. R. Link, T. Gao, R. E. Betts, S. H. Reiver, V. Chin, S. N. Bhatia, M. J. Sailor, *Science* **2003**, *299*, 2045.

[28] S. Y. Choi, M. Mamak, G. von Freymann, N. Chopra, G. A. Ozin, *Nano Lett.* **2006**, *6*, 2456.

[29] M. E. Calvo, S. Colodrero, N. Hidalgo, G. Lozano, C. Lopez-Lopez, O. Sanchez-Sobrado, H. Miguez, *Energy Environ. Sci.* **2011**, *4*, 4800.

[30] F. Cunin, T. A. Schmedake, J. R. Link, Y. Y. Li, J. Koh, S. N. Bhatia, M. J. Sailor, *Nat. Mater.* **2002**, *1*, 39.

[31] J. Kobler, B. V. Lotsch, G. A. Ozin, T. Bein, *ACS Nano* **2009**, *3*, 1669.

[32] S. Colodrero, A. Mihi, L. Haggman, M. Ocana, G. Boschloo, A. Hagfeldt, H. Miguez, *Adv. Mater.* **2009**, *21*, 764.

[33] Y. Yamada, T. Nakamura, M. Ishi, K. Yano, *Langmuir* **2006**, *22*, 2444.

[34] H. Yamada, T. Nakamura, Y. Yamada, K. Yano, *Adv. Mater.* **2009**, *21*, 4134.

[35] M. C. Fuertes, F. J. Lopez-Alcaraz, M. C. Marchi, H. E. Troiani, V. Luca, H. Miguez, G. J. A. A. Soler-Illia, *Adv. Funct. Mater.* **2007**, *17*, 1247.

[36] K. E. Shopsowitz, H. Qi, W. Y. Hamad, M. J. MacLachlan, *Nature* **2010**, *468*, 422.

[37] K. E. Shopsowitz, W. Y. Hamad, M. J. MacLachlan, *J. Am. Chem. Soc.* **2012**, *134*, 867.

[38] K. E. Shopsowitz, W. Y. Hamad, M. J. MacLachlan, *Angew. Chem. Int. Ed.* **2011**, *50*, 10991.

[39] K. E. Shopsowitz, A. Stahl, W. Y. Hamad, M. J. MacLachlan, *Angew. Chem. Int. Ed.* **2012**, *51*, 6886.

[40] W. Y. Hamad, T. Q. Hu, *Can. J. Chem. Eng.* **2010**, *88*, 392.

[41] J. A. Kelly, M. Yu, W. Y. Hamad, M. J. MacLachlan, *Adv. Opt. Mater.* **2013**, *1*, 295.

[42] J. Majoinen, E. Kontturi, O. Ikkala, D. G. Gray, *Cellulose* **2012**, *19*, 1599.

[43] C. J. Brinker, Y. F. Lu, A. Sellinger, H. Y. Fan, *Adv. Mater.* **1999**, *11*, 579.

[44] a) M.-C. B. Salon, G. Gerbaud, M. Abdelmouleh, C. Bruzzese, S. Boufi, M. N. Belgacem, *Magn. Reson. Chem.* **2007**, *45*, 473; b) M. Abdelmouleh, S. Boufi, A. ben Salah, M. N. Belgacem, A. Gandini, *Langmuir* **2002**, *18*, 3203.

[45] A. Bertoluzza, C. Fagnano, M. A. Morelli, V. Gottardi, M. Guglielmi, *J. Non-Cryst. Solids* **1982**, *48*, 117.

[46] F. Rouquerol, J. Rouquerol, K. Sing, in *Adsorption by Powders and Porous Solids*, Academic Press, London, **1999**, Ch. 4.

[47] M. C. Burleigh, M. A. Markowitz, S. Jayasundera, M. S. Spector, C. W. Thomas, B. P. Gaber, *J. Phys. Chem. B* **2003**, *107*, 12628.

[48] K. Robbie, D. J. Broer, M. J. Brett, *Nature* **1999**, *399*, 764.

[49] I. B. Burgess, N. Koay, K. P. Raymond, M. Kolle, M. Loncar, J. Aizenberg, *ACS Nano* **2012**, *6*, 1427.

[50] M. A. Anderson, A. Tinsley-Bown, P. Allcock, E. A. Perkins, P. Snow, M. Hollings, R. G. Smith, C. Reeves, D. J. Squirrell, S. Nicklin, T. I. Cox, *Phys. Stat. Solidi A* **2003**, *197*, 528.